Article

Crystal Structures of Botulinum Neurotoxin Subtypes A4 and A5 Cell Binding Domains in Complex with Receptor Ganglioside

Kyle S. Gregory [1], Otsile O. Mojanaga [1], Sai Man Liu [2] and K. Ravi Acharya [1,*]

[1] Department of Biology and Biochemistry, University of Bath, Claverton Down, Bath BA2 7AY, UK; kg540@bath.ac.uk (K.S.G.); oom21@bath.ac.uk (O.O.M.)

[2] Protein Sciences Department, Ipsen Bioinnovation Limited, 102 Park Drive, Milton Park, Abingdon OX14 4RY, UK; sai.man.liu@ipsen.com

* Correspondence: bsskra@bath.ac.uk; Tel.: +44 (0) 1225 386238

Abstract: Botulinum neurotoxins (BoNT) cause the potentially fatal neuroparalytic disease botulism that arises due to proteolysis of a SNARE protein. Each BoNT is comprised of three domains: a cell binding domain (H_C), a translocation domain (H_N), and a catalytic (Zn^{2+} endopeptidase) domain (LC). The H_C is responsible for neuronal specificity by targeting both a protein and ganglioside receptor at the neuromuscular junction. Although highly toxic, some BoNTs are commercially available as therapeutics for the treatment of a range of neuromuscular conditions. Here we present the crystal structures of two BoNT cell binding domains, H_C/A4 and H_C/A5, in a complex with the oligosaccharide of ganglioside, GD1a and GM1b, respectively. These structures, along with a detailed comparison with the previously reported apo-structures, reveal the conformational changes that occur upon ganglioside binding and the interactions involved.

Keywords: botulinum neurotoxin; crystal structure; cell binding domain; subtypes A4 and A5; ganglioside binding

Key Contribution: Botulinum neurotoxin type A is a therapeutically important BoNT serotype. Crystal structures of both BoNT/A4 and /A5 in a complex with GD1a and GM1b gangliosides, respectively, reveal the residues involved in binding and the conformational changes that occur upon binding.

1. Introduction

Botulinum neurotoxin serotype A (BoNT/A) is produced by anaerobic spore forming bacteria, *Clostridium botulinum*, and, along with other serotypes, is responsible for the disease *botulism*—a neuromuscular condition that causes flaccid paralysis and can lead to death by asphyxiation if left untreated [1]. The exquisite toxicity of BoNT/A makes it one of the deadliest agents known to humankind [2]; however, at miniscule doses, they can be used as a therapeutic to treat a range of diseases associated with hyper-muscular and -glandular activity [3]. The toxin is post-translationally cleaved to form an active di-chain, comprised of a 50 kDa light chain (LC) and a 100 kDa heavy chain (HC) linked by a disulphide bond. The HC can be further divided into an N-terminal translocation domain (H_N) and a C-terminal cell binding domain (H_C) [4]. The mechanism of intoxication involves three general steps [5]: highly specific targeting to the neuromuscular junction by dual-receptor recognition of both a protein and ganglioside receptor by the H_C domain, resulting in endocytic internalisation into an endosome [6]; pH-mediated conformational change of the H_N domain that translocates the LC into the cytosol [7–9]; and a Zn^{2+}-dependent endopeptidase cleavage of a soluble *N*-ethylmaleimide-sensitive factor attachment protein receptor (SNARE) protein by the LC [10]. This cleavage prevents vesicular fusion to the cell membrane, halting the release of

presynaptic acetylcholine, and the progression of synaptic signalling at the neuromuscular junction [11].

There are many different types of BoNT and BoNT-like molecules that are categorised by sequence similarity, serological activity, and/or host source. BoNTs produced by Clostridia are categorised into serotypes /A to /G, and /X, whereas the BoNT-like molecules by non-Clostridia include BoNT/Wo (*Weissella oryzae*) [12], BoNT/En (*Enterococcus faecium*) [13], and PMP1 (*Paraclostridium bifermentans*) [14]. Some serotypes exist naturally as mosaics (e.g., BoNT/CD, BoNT/DC, and BoNT/FA), whereas other serotypes are divided into subtypes (e.g., BoNT/A1-/A8, /B1-/B8, /E1-/E12, /F1-/F9) due to subtle variations in amino acid sequence [15,16]. Although these subtypes arise due to only minor changes in their amino acid sequence, the toxicity of subtypes has been shown to vary significantly [17–20]. All serotypes require recognition of both a protein (Synaptic vesicle protein 2 in BoNT/A) and ganglioside receptor to initiate endocytosis, except for BoNT/C which binds to two gangliosides. Gangliosides are glycosphingolipids that are often involved in cellular-signalling pathways and are comprised of a membrane anchored hydrophilic lipid tail, and an extracellular oligosaccharide moiety [21]. Previous studies have reported the structures of the binding domain of BoNT/A1 (H_C/A1) and BoNT/A3 (H_C/A3) in complex with the receptor ganglioside GD1a [22,23], detailing the interactions that occur between the two. These structures reveal that the ganglioside binding site (GBS) is formed by a β-hairpin and loop in the C-terminal subdomain of H_C (H_{CC}).

We have previously reported the crystal structures of H_C/A4 [24] and H_C/A5 [25], and now present the crystal structures of H_C/A4 in complex with GD1a, and H_C/A5 in complex with GM1b, and highlight the interactions and structural changes that occur upon ganglioside binding. The structural information revealed in this report may aid in the development of future BoNT therapeutics.

2. Results and Discussion

2.1. Structure of H_C/A4 in Complex with GD1a Oligosaccharide

The structure of the H_C/A4:GD1a complex was solved to 2.3 Å by molecular replacement using the unbound H_C/A4 structure (PDB: 6F0P) [24] as a search model. Two molecules (designated A and B) were present in the asymmetric unit (ASU) (Table 1). The overall quality of the electron density map was good with better density for molecule A (residues 994-999, 1029-1032,1047-1053, 1172-1174, and 1232-1239 could not be modelled for molecule B). Consequently, all subsequent analyses below involved molecule A. An initial inspection of the map revealed large positive electron density at the expected GBS, which indicated that GD1a had bound. Monosaccharides Sia^5-Gal^2 could be modelled with no ambiguity into the electron density (Figure 1A) and Glc^1 partially, but there was insufficient electron density to model Sia^6. A total of nine hydrogen bonding interactions were present between H_C/A4 and GD1a (Figure 1B) (Table 2)—there was clear electron density for the two terminal nitrogen atoms of Arg 1282 which interact with Sia^5 and Gln 1276.

Table 1. X-ray crystallographic data collection and refinement statistics for H_C/A4:GD1a and H_C/A5:GM1b. Outer shell statistics are in parentheses.

Beamline	I04	
Wavelength used	0.9795 Å	
Protein	**H_C/A4:GD1a**	**H_C/A5:GM1b**
Crystallographic Statistics		
Space group	$P6_1$	$P2_1$
Unit cell dimensions:		
a, b, c (Å)	94.68, 94.68, 181.21	44.16, 129.40, 78.05

α, β, γ (°)	90.00, 90.00, 120.00	90.00, 102.96, 90.00
Resolution range (Å)	90.60–2.30 (2.38–2.30)	129.40–2.30 (2.49–2.40)
R_{merge}	0.269 (1.866)	0.305 (1.586)
R_{pim}	0.043 (0.366)	0.126 (0.746)
$<I/\sigma(I)>$	12.1 (1.9)	4.3 (0.8)
$CC_{1/2}$	0.998 (0.644)	0.982 (0.575)
Completeness (%)	99.7 (97.5)	100.0 (100.0)
No. observed reflections	1,594,764 (97,629)	227,781 (22,543)
No. unique reflections	40,672 (3,862)	33,451 (3,528)
Multiplicity	39.2 (25.3)	6.8 (6.4)
Refinement Statistics		
R_{work}/R_{free}	0.203/0.248	0.222/0.262
RMSD bond lengths (Å)	0.004	0.003
RMSD bond angles (°)	0.68	0.55
Ramachandran plot statistics (%):		
Favoured	95.44	95.38
Allowed	4.56	4.34
Outliers	0.00	1.02
Average B-Factors (Å²):		
Protein atoms	42.28	39.10
Solvent atoms	35.04	32.36
GD1a atoms	72.59	70.99
No. Atoms:	7,069	6,286
Protein	6,696	6,094
Solvent	237	160
GD1a/GM1b carbohydrates	136	32
PDB code	7QPT	7QPU

Table 2. Hydrogen bonds for ganglioside binding in structures Hc/A4:GD1a and Hc/A5:GM1b (this study), compared to Hc/A3:GD1a (PDB: 6THY [23]) and Hc/A1:GD1a (PDB: 5TPC [22]). Water-mediated interactions are indicated by a "-H₂O molecule (n_1, n_2)" where n_1 is the distance between the amino acid residue and the water, and n_2 is the distance between the water and monosaccharide. △ Indicates they are the equivalent water molecule for each structure. Data adapted from [23].

| Monosaccharide	H-bonding residue (Distance in Å)			
	Hc/A5:GM1b	Hc/A4:GD1a	Hc/A3:GD1a	Hc/A1:GD1a
Sia[6]	N/A	Not modelled	Not modelled	Trp 1266 (3.5)
Sia[5]	Tyr 1117 (2.8)	Tyr 1123 (2.8)		Tyr 1117 (2.9)
	Tyr 1267 (2.7)	Tyr 1273 (2.5)	Tyr 1263 (2.7)	Tyr 1267-H₂O (2.5, 3.5)
	Gly 1279 (3.2)	Gly 1285 (3.1)	Gly 1275 (2.9)	Gly 1279-H₂O△ (2.6 2.8)
			Leu 1250-H₂O△ (2.9, 2.8)	
		Arg 1282 (3.8)		Arg 1276 -H₂O△ (2.8, 2.8)
Gal[4]	Glu 1203 (2.6)	Glu 1209 (2.4)	Glu 1199 (2.7)	Glu 1203 (2.8)
	Phe 1252 (2.8)	Phe 1258 (2.8)	Phe 1248 (2.5)	Phe 1252 (2.7)
	His 1253 (3.1)	His 1259 (2.7)	His 1249 (3.1)	His 1253 (2.7)
	Ser 1264 (2.9)	Ser 1270 (2.5)	Ser 1260 (2.7)	Ser 1264 (2.8)
			Leu 1250-H₂O△ (2.9, 3.0)	
GalNAc[3]	Not modelled	Glu 1209 (2.6)	Glu 1199 (2.5)	Glu 1203 (2.5)
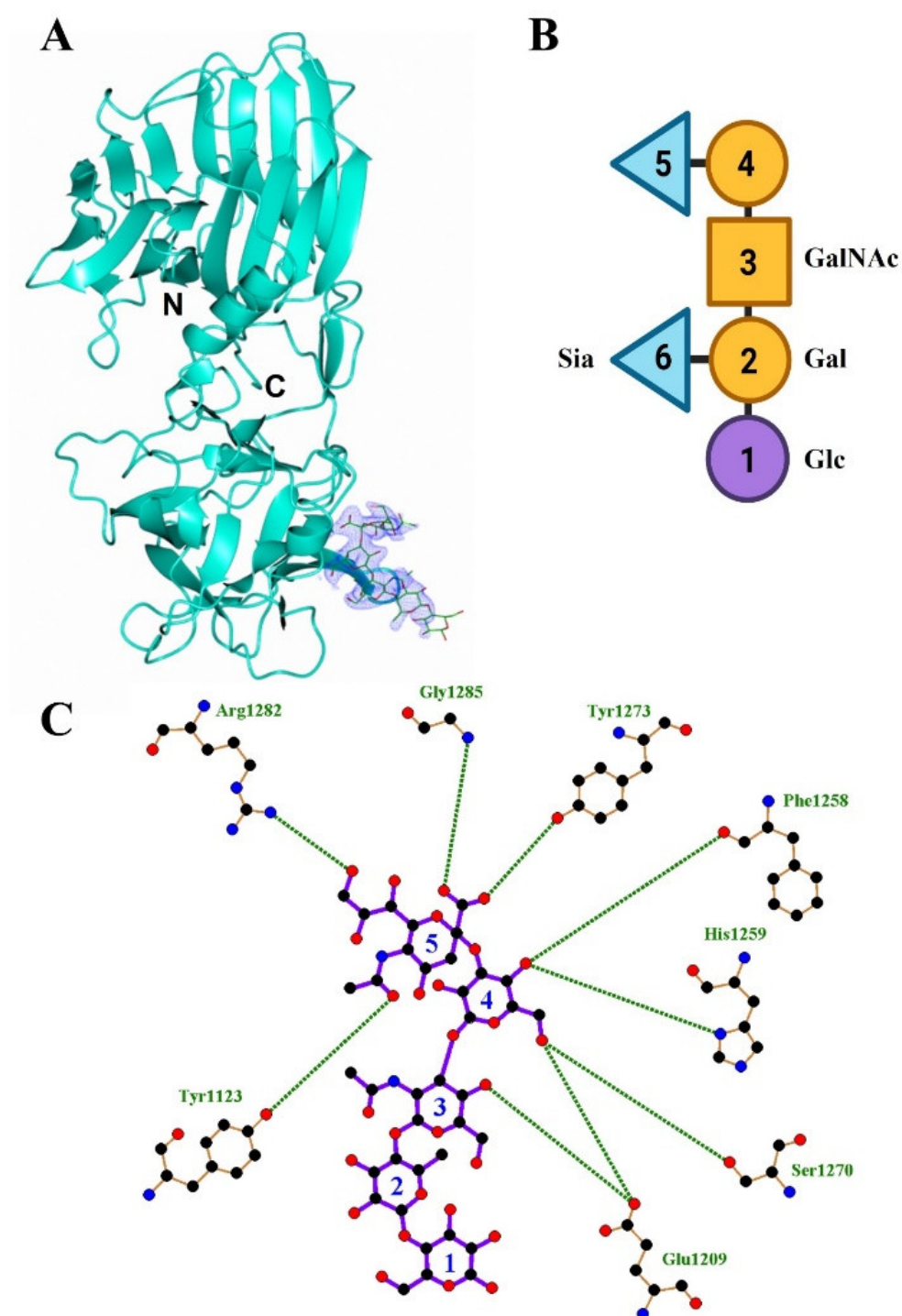
Figure 1. Structure of Hc/A4:GD1a. (**A**) Crystal structure of Hc/A4 in complex with GD1a oligo-saccharide, the electron density map of GD1a (2Fo-Fc) is contoured to 1 σ; (**B**) schematic diagram of GD1a ganglioside; (**C**) LigPlot of GD1a and Hc/A4 hydrogen bonding interactions.

The crystal packing of Hc/A4 changes significantly upon binding of GD1a as evidenced by the change in both unit cell dimensions and space group. Although there is minimal overall conformational change between Hc/A4:GD1a with Hc/A4 alone (RMSD of 0.88 Å for all Cα atoms); there is a noticeable change in the relative position of the Hc_N and Hc_C subdomains when compared to the unbound structure (RMSD of 0.6 and 0.5 Å, respectively, for all Cα atoms after individual subdomain superimposition). Therefore, upon ganglioside binding, the two subdomains appear to rotate apart like an opening

hinge (Figure 2A). There is also a noticeable conformational change to the loop spanning residues 933-946 within the H_{CN} subdomain (Figure 2A) that may be attributed to different crystal packing in the unbound structure.

Inspection of the H_C/A4:GD1a GBS residues revealed changes in the relative position of the side chains compared to H_C/A4 alone; most notably Arg 1282 (which adopts two conformations in the unbound structure) and Tyr 1123. Upon GD1a binding, these residues shift to form a hydrogen bonding interaction with Sia^5 (Figure 2B).
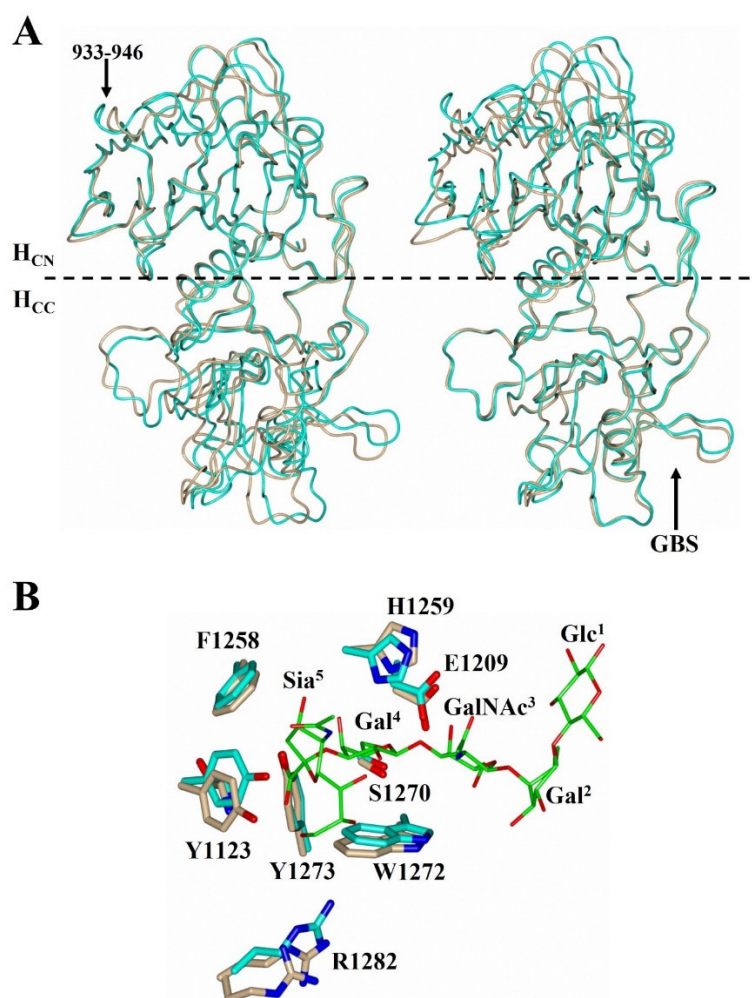
Figure 2. Comparison of H_C/A4:GD1a with H_C/A4. (**A**) Superimposition of the H_{CN} (left) and H_{CC} (right) domains of H_C/A4:GD1a (cyan) and H_C/A4 (burlywood; PDB: 6F0P [22]) shows a hinge movement between the subdomains; (**B**) Comparison of H_C/A4:GD1a and H_C/A4 at the ganglioside binding site.

## 2.2. Structure of H_C/A5 Co-crystallised with GM1b Oligosaccharide

Several attempts to crystallise H_C/A5 with GD1a did not yield crystals for the complex. Consequently, a smaller ganglioside, GM1b, which is identical to GD1a in terms of the expected binding portion (Sia^5-$GalNAc^3$) but lacks only Sia^6 (Figure 1B), was used for co-crystallisation with H_C/A5. Crystals of H_C/A5:GM1b diffracted to 2.4 Å, in space group $P2_1$ (Table 1), and the structure was determined by molecular replacement with two molecules (designated A and B) in the ASU (Figure 3A). Molecule A generally showed clearer electron density throughout the structure compared to molecule B, especially the H…SxWY motif that is essential for ganglioside binding [26] which could not be modelled in molecule B. There are, however, three small loop regions in molecule A (1167-1169, 1226-1235, and 1271-1276) that showed insufficient density for modelling. It

is possible that the latter loop (residues 1271-1276) is flexible due to its proximity to the GBS.

Both molecules A and B are conformationally very similar, with an RMSD of 0.68 Å for all Cα atoms. Residues 928-939, however, adopt alternative conformations - for molecule A they form a β-strand with residues 1047-1050 of the conserved jelly-roll fold, whereas for molecule B, they form an unstructured loop (Figure 3C). Inspection of the surrounding symmetry-related molecule suggests that this difference may be due to crystallographic packing.

The two molecules of the ASU form a dimer through an extended β-sheet interaction (Figure 3A, Arrow). For the interaction to occur the 882-889 loop, which extends beyond the β-sheet (Figure 4C, Arrow), has to move away to allow for the interface to form between molecule A and B. Although computational analyses [27] suggest this may also be due to crystallographic packing, the GBS in this crystal form has become accessible to ligand binding. For molecule A, some additional weak electron density was observed at the GBS that was not part of the protein. With the aid of polder maps [28] for His 1253 and Tyr 1117 [22,23,29], it was possible to model in sugars Gal^4 and Sia^5 (Figure 3B). Gal^4 forms a total of four hydrogen bonds with residues Glu 1203, Phe 1252, His 1253, and Ser 1264, while Sia^5 forms three hydrogen bonds with Tyr 1117, Tyr 1267, and Gly 1279 (Table 2). Further refinement of the Gal^4 molecule with occupancies 0.6 and 1 generated average B-factors of 60.74 $Å^2$ and 61.97 $Å^2$, respectively, indicating that GM1b is bound at low occupancy.
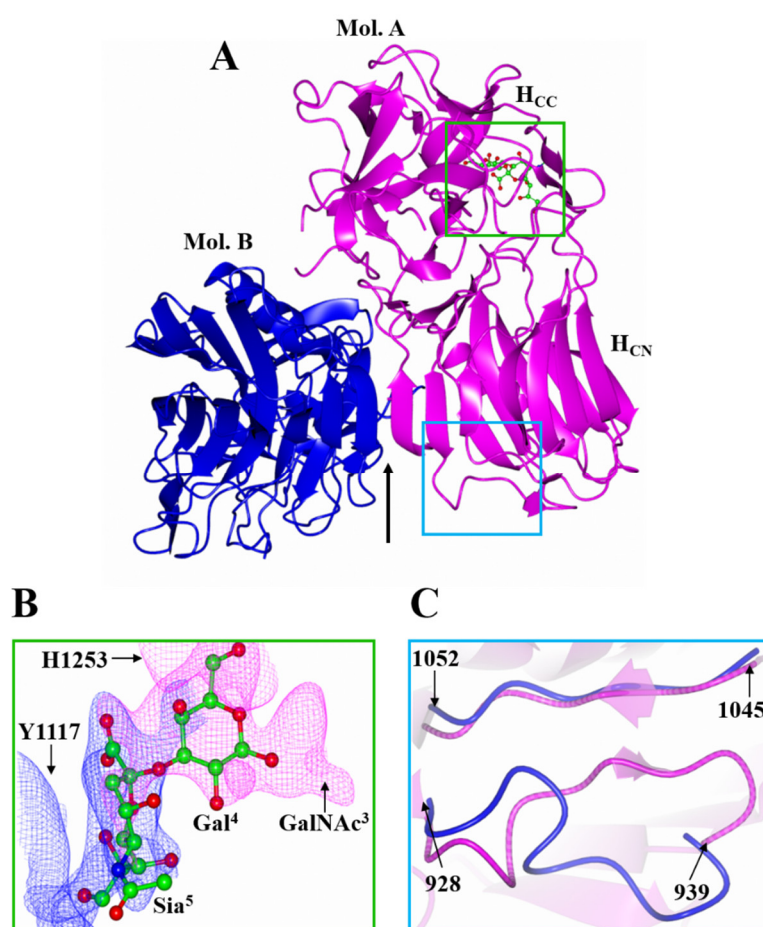

Figure 3. Crystal structure of Hc/A5:GM1b. (**A**) The structure of Hc/A5:GM1b was solved with two molecules in the ASU designated 'A' (magenta) and 'B' (blue). The arrow indicates the location of the crystallographic dimer interface; (**B**) Ganglioside binding site of molecule 'A'. The polder maps for Gal^4 (magenta) and Sia^5 (blue) are contoured to 3 σ. His 1253 and Tyr 1117 have been

omitted for clarity; (**C**) Superimposition of molecule 'A' and 'B' shows a change in conformation of the loop spanning residues 928-939.

The β-sheet arrangement between the two molecules of the ASU, shows a significant conformational change at the N-terminus of the H$_C$/A5:GM1b structure when compared to H$_C$/A5 alone (Figure 4C,D). Most prominently, the side chains of Arg 893 and Tyr 894 have rotated towards the main body of the protein structure upon GM1b binding, and there is a rotation in the protein backbone that results in a more compact structure. This closely resembles the full-length structure of BoNT/A1 (PDB:3BTA) in the absence of ganglioside.

Overall, the H$_C$/A5:GM1b structure is very similar to the H$_C$/A5 structure (PDB:6TWP), with RMSD values of 0.76 Å (for Cα atoms) for molecule A and 0.64 Å for molecule B (for Cα atoms). Considering that the residues of the GBS for molecule B could not be modelled, comparisons to the unbound H$_C$/A5 structure will be made with molecule A. Most of the residues within the putative GBS show little to no conformational change, with the exception of Phe 1278 which has its side chain flipped towards the GBS (Figure 4A,B). This flip in residue positioning is accompanied by a change in the loop structure spanning residues 1260–1280, where there is an increase in the Cα distance of 4 Å between residues Tyr 1267 and Thr 1277 upon ganglioside binding (Figure 4A and B inset). This increase in Cα distance is indicative of the loop widening to accommodate the ganglioside.
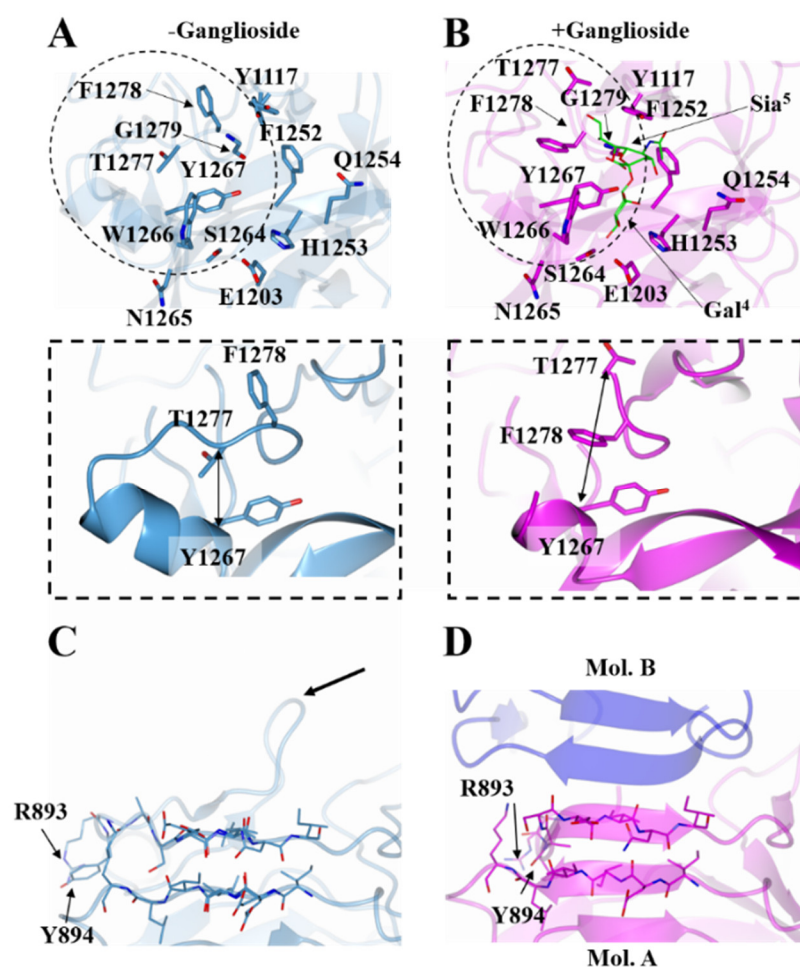
**Figure 4.** Comparison of H$_C$/A5:GM1b with H$_C$/A5. Structure of the GBS of H$_C$/A5 with and without GM1b oligosaccharide (**B** and **A** (PDB: 6TWP [22]), respectively). The widening of the loop region spanning residues 1260-1280 is indicated by double-headed arrows (*inset*). Structure of H$_C$/A5

N-terminus with and without GM1b oligosaccharide (**D** and **C**, respectively). The former shows the crystallographic dimer interface between molecule 'A' (magenta) and 'B' (blue). Arrow points to the location of loop 882-889.

2.3. Structural Variability of H$_C$/A Subtypes at the Ganglioside Binding Site

There appears to be some structural variation of the GBS among the H$_C$/A subtypes as illustrated by a comparison of the H$_C$/A1, H$_C$/A3, H$_C$/A4, and H$_C$/A5 structures with and without ganglioside bound (Figure 5). The most significant variation is seen within the loop that follows the β-hairpin of the GBS for H$_C$/A3 and H$_C$/A5 (Figure 6A–D, Arrow). Upon binding the ganglioside, the loop widens in H$_C$/A3 and H$_C$/A5, as measured by an increase in the distance between Cα atoms of T1273^{A3}/1277^{A5} and Y1263^{A3}/1267^{A5} within the loop, to accommodate the ganglioside. In contrast, the loop in the unbound H$_C$/A1 and H$_C$/A4 structures, adopts a more open conformation, which suggests that it does not need to move to allow GD1a to bind. Furthermore, a comparison of the GBS opening groove, formed by the histidine and tryptophan residues of the H…SxWY motif, in the bound and unbound structures reveals that the structural changes of H$_C$/A4 is more similar to H$_C$/A1 than H$_C$/A3, with the tryptophan moving towards the GBS upon ganglioside binding (Figure 7A–D). H$_C$/A5 is somewhere in between with some conformational variation reminiscent of the H$_C$/A3 structure, where Phe 1274^{A3}/1278^{A5} appears to flip towards the GBS upon binding. This residue is not conserved across the subtypes—it appears as Leu 1278 for H$_C$/A1 and Leu 1285 for H$_C$/A4. Not surprisingly, there is some variation to the ganglioside interaction between subtypes. H$_C$/A1 has a total of ten hydrogen bonding interactions with GD1a, while H$_C$/A3 and /A4 has nine (Table 2). Furthermore, H$_C$/A4 displays no water-mediated interactions with the ganglioside, while both H$_C$/A1 and H$_C$/A3 have at least two each. The occupancy of Gal^4 and Sia^5 in the H$_C$/A5:GM1b structure was too low to be able to determine any water-mediated interactions that contributed to binding.
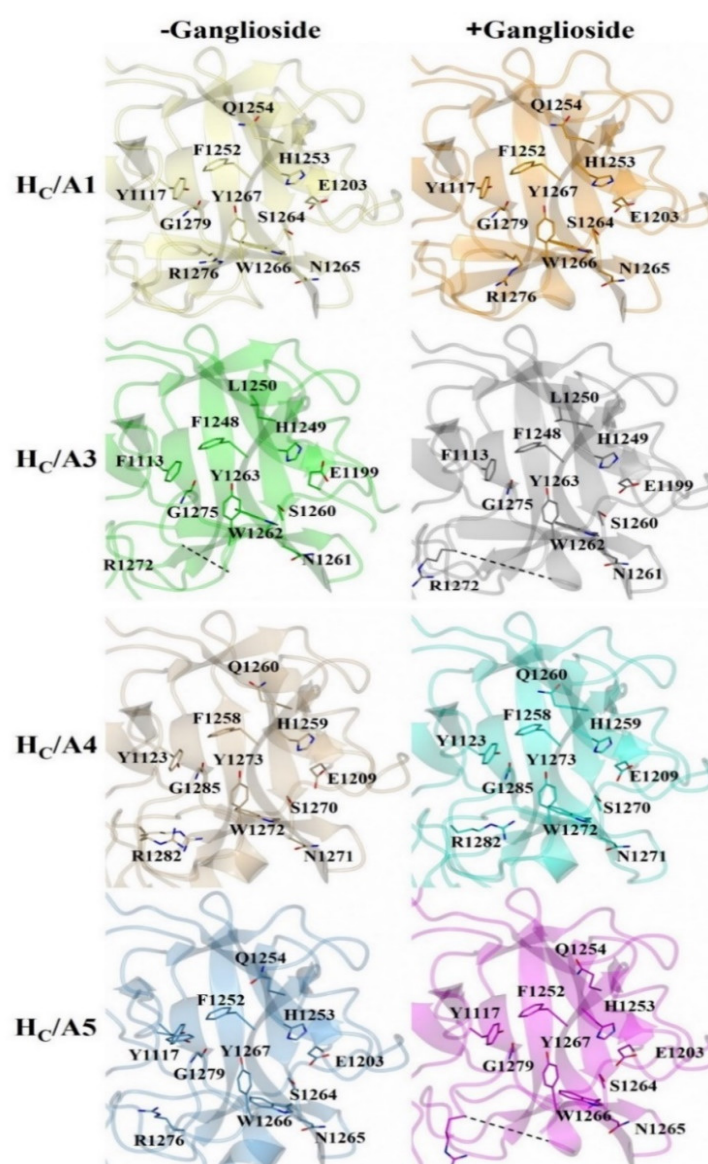
Figure 5. Structural comparison of the ganglioside binding site with and without oligosaccharide. H$_C$/A1 (PDB: 2VUA [29]), H$_C$/A1:GD1a (PDB: 5TPC [22]), H$_C$/A3 (PDB: 6F0O [22]), H$_C$/A3:GD1a (PDB: 6THY [22]), H$_C$/A4 (PDB: 6F0P [24]), H$_C$/A4:GD1a (this study), H$_C$/A5 (PDB: 6TWP [24]), and H$_C$/A5:GM1b (this study).
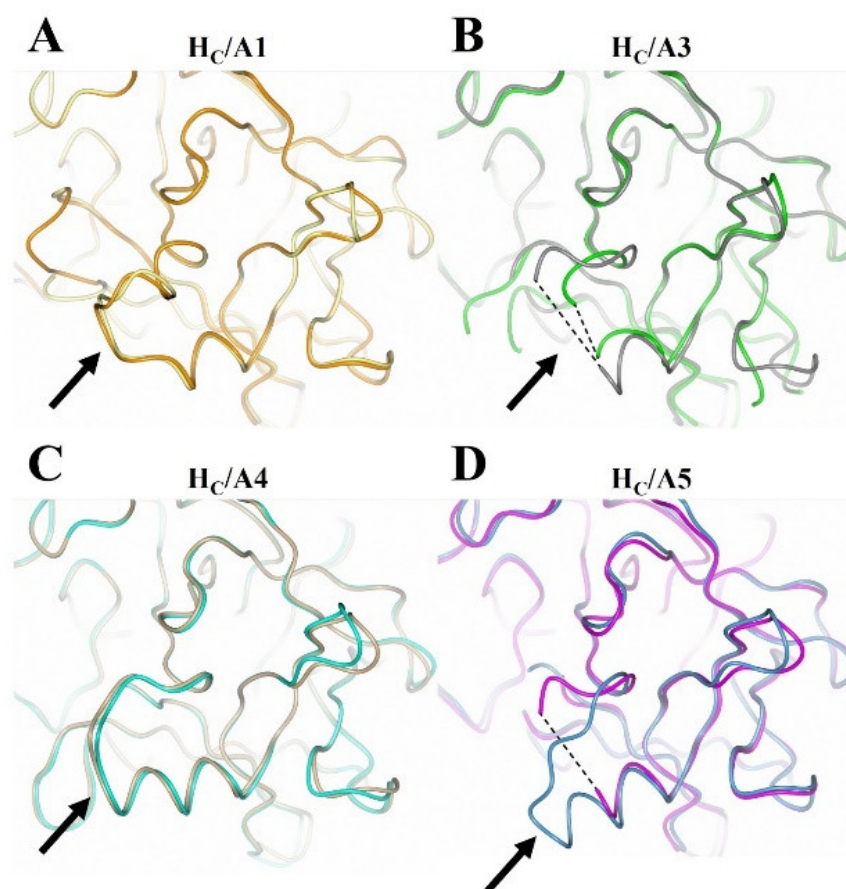
Figure 6. Structural comparison of the loop that follows the β-hairpin of the ganglioside binding site with and without oligosaccharide. (**A**) H$_C$/A1 unbound (yellow; PDB: 2VUA [29]) and bound to GD1a (orange; PDB: 5TPC [22]); (**B**) H$_C$/A3 unbound (green; PDB: 6F0O [24]) and bound to GD1a (dark grey; PDB: 6THY [23]); (**C**) H$_C$/A4 unbound (burlywood; PDB: 6F0P [24]) and bound to GD1a (cyan; this study); (**D**) H$_C$/A5 unbound (grey; PDB: 6TWP [25]) and bound to GM1b (cyan; this study). The arrow points to the loop that follows the GBS-β hairpin; dotted lines indicate un-modeled regions of the loop.
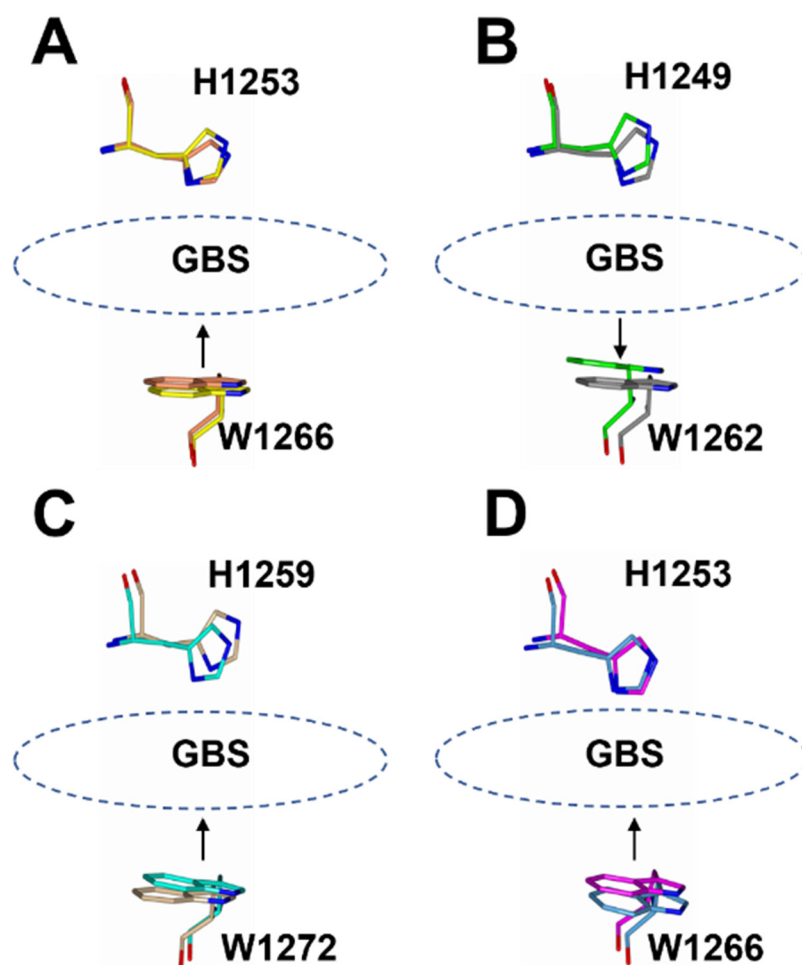
Figure 7. Superimposition of the opening groove between His and Trp residues of the GBS for ganglioside bound and unbound Hc/A subtypes. For Hc/A1 (**A**), Hc/A4 (**C**), and Hc/A5 (**D**), the Trp residue moves towards the His residue, whereas for Hc/A3 (**B**) it moves away.

3. Conclusions

The crystal structures of Hc/A4:GD1a and Hc/A5:GM1b presented here reveal the interactions involved with ganglioside binding and also the conformational changes that occur. For Hc/A4, eight residues form a total of nine hydrogen bonding interactions with the three principal oligosaccharides, GalNAC[3], Gal[4], and Sia[5]. However, for Hc/A5, only two oligosaccharides could be modelled in the electron density map, revealing seven hydrogen bonding interactions. The low occupancy of GM1b, and multiple failed attempts of co-crystallising Hc/A5 with GD1a, suggested a low affinity to the Sia-Gal-GalNAc moiety or preference for a different ganglioside.

A total of four Hc/A subtype structures (Hc/A1, Hc/A3, Hc/A4, Hc/A5) have now been reported with and without ganglioside. We previously reported that the reduction in hydrogen bonding interactions of Hc/A3 for GD1a compared to Hc/A1, may be a contributing factor in its reduction in toxicity [23]. Hc/A4 follows this trend as the structure displays a reduction in hydrogen bonding interactions with GD1a and has a reported 1,000-fold lower activity in mice [30]. Furthermore, both BoNT/A3 and BoNT/A4 are significantly less active in vivo when compared to BoNT/A1, and BoNT/A4 is also less efficient at entering cells [31], with the cell binding domain contributing to this variation.

4. Materials and Methods

All reagents were purchased from Sigma-Aldrich (St. Loius, Missouri, United States), Fischer Scientific (Loughborough, UK), and Molecular Dimensions (Newmarket, UK) unless otherwise stated. GD1a and GM1b oligosaccharides were supplied by Elicityl (Crolles, France).

4.1. Protein Expression and Purification

The sequences of BoNT/A4 residues 870-1296 (HC/A4) and BoNT/A5 residues 871-1296 (HC/A5) were cloned into the pJ401 vector with an N-terminal hexa-histidine tag, as described previously [24,25]. Both constructs were transformed into *E. coli* strain BL21 and grown at 37 °C to an OD600 of 0.5 before induction with 1 mM IPTG for 16 h at 16 °C. Cells were harvested by centrifugation. Cells expressing H_C/A4 were lysed in 50 mM Tris pH 7.4, 0.2 M NaCl, 10 mM trehalose and 20 mM imidazole, while cells expressing H_C/A5 were lysed in 50 mM Tris pH 7.4, 0.5 M NaCl, and 20 mM imidazole. Both proteins were captured on a GE HisTrap column and further purified by gel filtration using a GE superdex 200 column. For H_C/A4, the running buffer was 50 mM Tris pH 7.4, 150 mM NaCl, and 10 mM trehalose, while for H_C/A5 it was 50 mM Tris pH 7.4 and 150 mM NaCl. Both proteins were concentrated to 1 mg/mL using a 10 kDa MWCO centrifugal concentrator and flash frozen in liquid nitrogen for storage at −20 °C until required for crystallisation.

4.2. Protein Crystallisation

H_C/A4 and H_C/A5 proteins were concentrated to 5 mg/mL and the former incubated with 5 mM GD1a oligosaccharide and the latter with 5 mM GM1b oligosaccharide for 1 h at room temperature. Crystallisation screens were setup using the sitting drop vapour diffusion method in 96-3 well intelli-plates (SWISSCI, High Wycombe, UK) with a number of high throughput crystallisation conditions (Molecular Dimensions). Both a 1:1 and 2:1 protein to reservoir ratios were screened in each case. H_C/A4 crystals grew in 0.2 M NaAcO·3H$_2$O, 20% w/v PEG 3350 (1:1 ratio, protein:reservoir). H_C/A5 crystals grew in 150 mM Li$_2$SO$_4$, 50 mM MgCl$_2$·6H$_2$O, 0.1 M HEPES pH 7.8, 4.7% w/v PEG 8K, 4.7% PEG 10K and 4.7% PEG 8K (1:1 ratio, protein:reservoir). Crystals were mounted directly onto a cryo-loop and flash frozen for storage in liquid nitrogen.

4.3. X-ray Diffraction Data Collection and Structure Determination

Diffraction images were collected at a wavelength of 0.9785 Å with 0.1° oscillation and 0.01 s of exposure time per image on the i04 beamline at the Diamond Light Source (Harwell, Oxfordshire, UK). Crystals were kept under a jet stream of liquid nitrogen at 100 K during data collection. A total of 7200 images were collected for H_C/A4:GD1a, and 3600 images for H_C/A5:GM1b. Data processing was carried out in DIALS [32] and both structures were solved by molecular replacement in PHASER [33] using a previously reported structure of H_C/A4 [24] and H_C/A5 [25] as search models. Initial rounds of refinement were performed using REFMAC [26] as part of the CCP4 package [34] with the final round of refinement and validation performed in Phenix [35]. The structures were validated using Molprobity [36] and PDB validation. Figures were produced using ccp4mg [37] and BioRender.com (Biorender, Toronto, Canada).

Author Contributions: K.S.G. purified H_C/A5, performed all crystallographic analysis, wrote the manuscript, and supervised O.O.M.. O.O.M. performed purification, crystallisation, and preliminary crystallographic analysis of H_C/A4. S.M.L. analysed the data and edited the manuscript. K.R.A. supervised the study, analysed the data, and edited the manuscript. All authors have read and agreed to the published version of the manuscript.

References

1. Hatheway, C.L. Toxigenic clostridia. *Clin. Microbiol. Rev.* **1990**, *3*, 66–98.
2. Gill, D.M. Bacterial toxins: A table of lethal amounts. *Microbiol. Rev.* **1982**, *46*, 86–94.
3. Fonfria, E.; Maignel, J.; Lezmi, S.; Martin, V.; Splevins, A.; Shubber, S.; Kalinichev, M.; Foster, K.; Picaut, P.; Krupp, J. The expanding therapeutic utility of botulinum neurotoxins. *Toxins* **2018**, *10*, 208. https://doi.org/10.3390/toxins10050208.
4. Lacy, D.B.; Tepp, W.; Cohen, A.C.; DasGupta, B.R.; Stevens, R.C. Crystal structure of botulinum neurotoxin type A and implications for toxicity. *Nat. Struct. Biol.* **1998**, *5*, 898–902.
5. Pellizzari, R.; Rossetto, O.; Schiavo, G.; Montecucco, C. Tetanus and botulinum neurotoxins: Mechanism of action and therapeutic uses. *Philos. Trans. R. Soc. B Biol. Sci.* **1999**, *354*, 259–268.
6. Foster, K.A. The dual-receptor recognition of botulinum neurotoxins. In *Molecular Aspects of Botulinum Neurotoxin*; Springer: Berlin, Germany, 2014; pp. 129–150.
7. Schmid, M.F.; Robinson, J.P.; Dasgupta, B. Direct visualization of botulinum neurotoxin-induced channels in phospholipid vesicles. *Nature* **1993**, *364*, 827–830.
8. Hoch, D.H.; Romero-Mira, M.; Ehrlich, B.E.; Finkelstein, A.; DasGupta, B.R.; Simpson, L.L. Channels formed by botulinum, tetanus, and diphtheria toxins in planar lipid bilayers: Relevance to translocation of proteins across membranes. *Proc. Natl. Acad. Sci. USA.* **1985**, *82*, 1692–1696.
9. Montal, M. Translocation of botulinum neurotoxin light chain protease by the heavy chain protein-conducting channel. *Toxicon* **2009**, *54*, 565–569.
10. Schiavo, G.; Rossetto, O.; Santucci, A.; DasGupta, B.R.; Montecucco, C. Botulinum neurotoxins are zinc proteins. *J. Biol. Chem.* **1992**, *267*, 23479–23483.
11. Lu, B. The destructive effect of botulinum neurotoxins on the SNARE protein: SNAP-25 and synaptic membrane fusion. *PeerJ* **2015**, *2015*, 1–13.
12. Tanizawa, Y.; Fujisawa, T.; Mochizuki, T.; Kaminuma, E.; Suzuki, Y.; Nakamura, Y.; Tohno, M. Draft genome sequence of Weissella oryzae SG25T, isolated from fermented rice grains. *Genome Announc.* **2014**, *2*, 3–4.
13. Brunt, J.; Carter, A.T.; Stringer, S.C.; Peck, M.W. Identification of a novel botulinum neurotoxin gene cluster in Enterococcus. *FEBS Lett.* **2018**, *592*, 310–317.
14. Contreras, E.; Masuyer, G.; Qureshi, N.; Chawla, S.; Dhillon, H.S.; Lee, H.L.; Chen, J.; Stenmark, P.; Gill, S.S. A neurotoxin that specifically targets Anopheles mosquitoes. *Nat. Commun.* **2019**, *10*, 2869.
15. Rasetti-Escargueil, C.; Lemichez, E.; Popoff, M.R. Variability of botulinum toxins: Challenges and opportunities for the future. *Toxins* **2018**, *10*, 374. https://doi.org/10.3390/toxins10090374.
16. Hill, K.K.; Smith, T.J.; Helma, C.H.; Ticknor, L.O.; Foley, B.T.; Svensson, R.T.; Brown, J.L.; Johnson, E.A.; Smith, L.A.; Okinaka, R.T.; et al. Genetic diversity among botulinum neurotoxin-producing clostridial strains. *J. Bacteriol.* **2007**, *189*, 818–832.
17. Davies, J.R.; Liu, S.M.; Acharya, K.R. Variations in the botulinum neurotoxin binding domain and the potential for novel therapeutics. *Toxins* **2018**, *10*, 421. https://doi.org/10.3390/toxins10100421.
18. Pellett, S.; Tepp, W.H.; Whitemarsh, R.C.M.M.; Bradshaw, M.; Johnson, E.A. In vivo onset and duration of action varies for botulinum neurotoxin A subtypes 1–5. *Toxicon* **2015**, *107*, 37–42.
19. Wang, D.; Krilich, J.; Pellett, S.; Baudys, J.; Tepp, W.H.; Barr, J.R.; Johnson, E.A.; Kalb, S.R. Comparison of the catalytic properties of the botulinum neurotoxin subtypes A1 and A5. *Biochim. Biophys. Acta-Proteins Proteom.* **2013**, *1834*, 2722–2728.
20. Arndt, J.W.; Jacobson, M.J.; Abola, E.E.; Forsyth, C.M.; Tepp, W.H.; Marks, J.D.; Johnson, E.A.; Stevens, R.C. A structural perspective of the sequence variability within botulinum neurotoxin subtypes A1–A4. *J. Mol. Biol* **2006**, *362*, 733–742.
21. Ledeen, R. (1985) Gangliosides of the neuron. *Trends Neurosci.* **1985**, *8*, 169–174.
22. Hamark, C.; Berntsson, R.P.A.; Masuyer, G.; Henriksson, L.M.; Gustafsson, R.; Stenmark, P.; Widmalm, G. (2017) Glycans confer specificity to the recognition of ganglioside receptors by botulinum neurotoxin A. *J. Am. Chem. Soc.* **2017**, *139*, 218–230.
23. Gregory, K.S.; Liu, S.M.; Acharya, K.R. Crystal structure of botulinum neurotoxin subtype A3 cell binding domain in complex with GD1a co-receptor ganglioside. *FEBS Open Bio.* **2020**, *10*, 298–305.
24. Davies, J.R.; Rees, J.; Liu, S.M.; Acharya, K.R. High resolution crystal structures of Clostridium botulinum neurotoxin A3 and A4 binding domains. *J. Struct. Biol.* **2018**, *202*, 113–117.
25. Davies, J.R.; Britton, A.; Liu, S.M.; Acharya, K.R.High-resolution crystal structures of the botulinum neurotoxin binding domains from subtypes A5 and A6. *FEBS Open Bio.* **2020**, *10*, 1474–1481.
26. Popoff, M.R.; Connan, C. Absorption and transport of botulinum neurotoxins. In *Molecular Aspects of Botulinum Neurotoxin*; Springer: Berlin, Germany, 2014; pp. 35–68.

27. Elez, K.; Bonvin, A.M.J.J.; Vangone, A. Biological vs. crystallographic protein interfaces: An overview of computational approaches for their classification. *Crystals* **2020**, *10*, 114. https://doi.org/10.3390/cryst10020114.

28. Liebschner, D.; Afonine, P.V.; Moriarty, N.W.; Poon, B.K.; Sobolev, O.V.; Terwilliger, T.C.; Adams, P.D. Polder maps: Improving OMIT maps by excluding bulk solvent. *Acta Crystallogr. Sect. D Struct. Biol.* **2017**, *73*, 148–157.

29. Stenmark, P.; Dupuy, J.; Imamura, A.; Kiso, M.; Stevens, R.C. Crystal structure of botulinum neurotoxin type A in complex with the cell surface co-receptor GT1b-insight into the toxin-neuron interaction. *PLoS Pathog.* **2008**, *4*, e1000129. https://doi.org/10.1371/journal.ppat.1000129.

30. Whitemarsh, R.C.M.; Tepp, W.H.; Johnson, E.A.; Pellett, S. Persistence of botulinum neurotoxin a subtypes 1-5 in primary rat spinal cord cells. *PLoS ONE* **2014**, *9*, e90252.

31. Whitemarsh, R.C.M.; Tepp, W.H.; Bradshaw, M.; Lin, G.; Pier, C.L.; Scherf, J.M.; Johnson, E.A.; Pellett, S. Characterization of botulinum neurotoxin A Subtypes 1 through 5 by investigation of activities in mice , in neuronal cell cultures , and in vitro. *Infect. Immun.* **2013**, *81*, 3894–3902.

32. Waterman, D.G.; Winter, G.; Gildea, R.J.; Parkhurst, J.M.; Brewster, A.S.; Sauter, N.K.; Evans, G. Diffraction-geometry refinement in the DIALS framework. *Acta Crystallogr. Sect. D Struct. Biol.* **2016**, *72*, 558–575.

33. McCoy, A.J.; Grosse-Kunstleve, R.W.; Adams, P.D.; Winn, M.D.; Storoni, L.C.; Read, R.J. Phaser crystallographic software. *J. Appl. Crystallogr.* **2007**, *40*, 658–674.

34. Winn, M.D.; Ballard, C.C.; Cowtan, K.D.; Dodson, E.J.; Emsley, P.; Evans, P.R.; Keegan, R.M.; Krissinel, E.B.; Leslie, A.G.W.; McCoy, A.; et al. Overview of the CCP4 suite and current developments. *Acta Crystallogr. Sect. D Biol. Crystallogr.* **2011**, *67*, 235–242.

35. Liebschner, D.; Afonine, P.V.; Baker, M.L.; Bunkoczi, G.; Chen, V.B.; Croll, T.I.; Hintze, B.; Hung, L.W.; Jain, S.; McCoy, A.J.; et al. Macromolecular structure determination using X-rays, neutrons and electrons: Recent developments in Phenix. *Acta Crystallogr. Sect. D Struct. Biol.* **2019**, *75*, 861–877.

36. Williams, C.J.; Headd, J.J.; Moriarty, N.W.; Prisant, M.G.; Videau, L.L.; Deis, L.N.; Verma, V.; Keedy, D.A.; Hintze, B.J.; Chen, V.B.; et al. MolProbity: More and better reference data for improved all-atom structure validation. *Protein Sci.* **2018**, *27*, 293–315.

37. McNicholas, S.; Potterton, E.; Wilson, K.S.; Noble, M.E.M. Presenting your structures: The CCP4mg molecular-graphics software. *Acta Crystallogr. Sect. D Biol. Crystallogr.* **2011**, *67*, 386–394.